Center for Turbulence Research
Proceedings of the Summer Program 2024

Compressibility and vibrational-excitation effects in hypersonic shock-turbulence interaction

By A. Cuadra†, C. T. Williams, M. Di Renzo‡ AND C. Huete†

The interaction of turbulence with shock waves significantly modulates the frequency and amplitude of hydrodynamic fluctuations encountered by aerospace vehicles in low-altitude hypersonic flight. In these high-speed flows, intrinsic compressibility effects emerge together with high-enthalpy phenomena in the form of internal-energy excitation. The present study specifically compares direct numerical simulation (DNS) and linear interaction analysis (LIA) to characterize the impact of density fluctuations and endothermic processes in Mach-5 canonical shock-turbulence interaction (STI). Both the numerical and theoretical approaches reveal that increasing upstream compressibility augments the turbulent kinetic energy (TKE) across the STI for varying turbulent Mach numbers. The effect of endothermicity is likewise assessed in each framework by introducing equilibrium vibrational excitation, which is shown to further amplify the TKE downstream of the shock.

1. Introduction

Shock-turbulence interactions (STIs) are prevalent in hypersonic flight, where turbulence from the vehicle boundary layer interacts with shock waves generated by variations in the fuselage geometry. The nature of the incoming turbulence, including its intensity, length scales and level of compressibility, plays a crucial role in determining how the shock wave deforms and amplifies the turbulence. These factors strongly influence the resulting flow structure, affecting heat transfer, drag and vehicle stability. By isolating the key mechanisms mediating the interaction between small-scale turbulence fluctuations and shock waves in hypersonic flight, the canonical STI problem facilitates detailed comparisons between fully nonlinear DNS and linear analyses.

Previous studies have primarily focused on canonical STI problems, where incompressible homogeneous isotropic turbulence (HIT), dominated by vorticity disturbances, encounters a supersonic planar shock (Lee *et al.* 1993). However, in hypersonic regimes, solenoidal fluctuations are accompanied by dilatational disturbances, and even modest levels of dilatational energy in the upstream turbulence can significantly impact STI dynamics (Jamme *et al.* 2002; Grube & Martín 2023).

Shock waves induce sharp changes in the thermochemical properties of the air. As the shock slows down the flow, the gas thermal energy rises, and at sufficiently high temperatures, intense intermolecular collisions activate modes of intramolecular energy storage (Clarke 1991). At very high stagnation enthalpies, these collisions can ultimately lead to molecular dissociation, electronic excitation and ionization. Although the general principles of these processes are established (Vincenti & Kruger 1965), the detailed kinetics and their interaction with turbulence is an active research topic (Urzay & Di Renzo 2021).

† Department of Thermal and Fluids Engineering, University Carlos III of Madrid, Spain
‡ Department of Engineering for Innovation, University of Salento, Italy

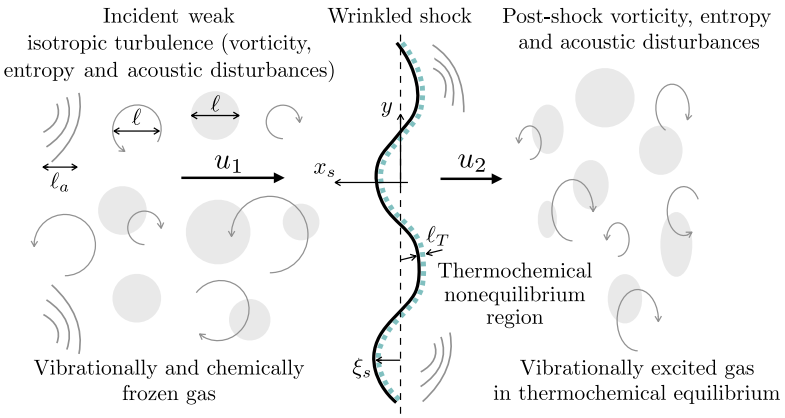

FIGURE 1. Sketch of the interaction of a planar shock wave with an isotropic vorticity-entropy-acoustic field in air at hypersonic speed (velocities are presented in the shock reference frame).

This study focuses on the STI problem, where compressible HIT is advected at hypersonic velocity toward the shock wave. Turbulence is comprised of acoustic, vortical, and entropic disturbances—with varying contributions from each mode—that impinge on the shock wave. This relatively simple configuration is analyzed using DNSs and LIA. In both cases, the effects of upstream turbulence compressibility and the potential impact of vibrational excitation of air molecules at Mach 5 are examined.

This paper is organized as follows. A brief description of the mathematical framework for the LIA and DNS is included in Sections 2 and 3. An analysis of the amplification of TKE across the shock is provided in Section 4. Final conclusions are given in Section 5.

2. Linear interaction analysis

The formulation utilized in the present study is largely consistent with that of Huete *et al.* (2021), where the upstream flow consisted solely of vortical disturbances. Here, the model is extended to account for density (Huete *et al.* 2011) and pressure (Huete *et al.* 2012) fluctuations in the upstream flow associated with acoustic, entropic, and vortical fluctuations, as depicted in Figure 1. Furthermore, endothermic effects in the form of vibrational excitation (Cuadra 2023; Cuadra *et al.* 2023) are also incorporated by solving the perturbation-free jump conditions across the shock using the Combustion Toolbox code (Cuadra *et al.* 2024).

Decomposing the upstream turbulence into vorticity-entropy and acoustic waves in a reference frame moving with the upstream mean flow (x, y), the streamwise velocity and density fluctuations can be expressed as

$$\delta u_1\left(x,y,t\right) = \varepsilon_r \langle c_1\rangle \cos\left(k_r x\right)\cos\left(k_y y\right) + \varepsilon_a \langle c_1\rangle \cos\left(k_a x - \omega_a t\right)\cos\left(k_y y\right), \tag{2.1a}$$

$$\delta \rho_1\left(x,y,t\right) = \varepsilon_e \langle \rho_1\rangle \cos\left(k_r x\right)\cos\left(k_y y\right) + \varepsilon_a \langle \rho_1\rangle \frac{\omega_a}{k_a}\cos\left(k_a x - \omega_a t\right)\cos\left(k_y y\right). \tag{2.1b}$$

In this formulation, $\langle c_1\rangle$ and $\langle \rho_1\rangle$ denote the mean speed of sound and density in the pre-shock gas, corresponding to the perturbation-free conditions. The dimensionless parameter ε_r denotes the pre-shock streamwise velocity-rotational fluctuation amplitude, assumed to be small in the linear theory, $\varepsilon_r \ll 1$. Characterized by a smaller level of intensity, the density-entropic fluctuation amplitude ε_e and the streamwise velocity-acoustic fluctuation amplitude ε_a are so defined. In the case considered in this work, the upstream

turbulent flow is dominated by the rotational disturbances so that ε_e and ε_a are smaller or much smaller than ε_r. However, their impact on the post-shock turbulent flow is not necessarily negligible, as will be demonstrated later. The numerical turbulence generator, employed later in the DNS study, will be used to compute the relative amplitude of the respective modes ahead of the shock.

The acoustic field demands the definition of the corresponding wave number k_a and frequency ω_a, which are related to each other through the sonic dispersion relationship $\omega_a^2 = c_1^2(k_a^2 + k_y^2)$. It is found convenient to define the wave angles $k_r/k_y = 1/|\tan\theta^r|$ and $k_a/k_y = 1/|\tan\theta^a|$. To perform the normal-mode analysis, it is found useful to write the upstream perturbation variables in the shock reference frame. Hence, the upstream excitation ahead of the shock translates into constant amplitude oscillations in the asymptotic long-time regime, where

$$\omega_s^r = \frac{\mathcal{R}\mathcal{M}_2}{\tan\theta^r} \quad \text{and} \quad \omega_s^a = \frac{\mathcal{R}\mathcal{M}_2}{\tan\theta^a}\left(1 - \frac{1}{\mathcal{M}_1\cos\theta^a}\right) \tag{2.2}$$

refer to the dimensionless shock oscillation frequencies produced by the upstream rotational-entropic and acoustic modes, respectively. In Eq. (2.2), $\mathcal{M}_1$ and $\mathcal{M}_2$ are the bulk upstream and downstream Mach numbers, and $\mathcal{R} = \rho_2/\rho_1$ is the shock density compression ratio. Thus, velocity, density and pressure perturbations right ahead of the shock, in terms of the dimensionless time $\tau = tk_yc_2$, take the form

$$\overline{u}_{1s}(\tau) = \frac{\delta u_{1s}}{\varepsilon_r c_1} = \cos(\omega_s^r\tau + \phi_r) + \frac{\varepsilon_a}{\varepsilon_r}\cos(\omega_s^a\tau + \phi_a), \tag{2.3a}$$

$$\overline{v}_{1s}(\tau) = \frac{\delta v_{1s}}{\varepsilon_r c_1} = \frac{k_r}{k_y}\sin(\omega_s^r\tau + \phi_r) - \frac{k_y}{k_a}\frac{\varepsilon_a}{\varepsilon_r}\sin(\omega_s^a\tau + \phi_a), \tag{2.3b}$$

$$\overline{\rho}_{1s}(\tau) = \frac{\delta\rho_{1s}}{\varepsilon_r\rho_1} = \frac{\varepsilon_e}{\varepsilon_r}\cos(\omega_s^r\tau + \phi_e) + \frac{\omega_a}{k_a}\frac{\varepsilon_a}{\varepsilon_r}\cos(\omega_s^a\tau + \phi_a), \tag{2.3c}$$

$$\overline{p}_{1s}(\tau) = \frac{\delta p_{1s}}{\varepsilon_r\rho_1 c_1^2} = \frac{\omega_a}{k_a}\frac{\varepsilon_a}{\varepsilon_r}\cos(\omega_s^a\tau + \phi_a), \tag{2.3d}$$

where the average symbol brackets $\langle\cdot\rangle$ have been omitted for clarity. In this formulation, ϕ_r, ϕ_e and ϕ_a denote the phases of the rotational, entropic and acoustic modes, respectively, and the subscript $1s$ defines upstream (subscript 1) disturbances at the shock (subscript s) location.

Once the upstream conditions are determined, the next step is to obtain the post-shock properties for the different perturbation modes. In a system of reference moving with the shock front immediately downstream from the perturbed shock surface (subscript 2), a corresponding set of perturbations is generated. For the velocity components, these downstream perturbations are evaluated as

$$\overline{u}_{2s}(\tau) = \frac{\delta u_{2s}}{\varepsilon_r c_2} = (\mathcal{U}_r^r + \mathcal{U}_a^r)\cos(\omega_s^r\tau + \phi_r) + (\mathcal{U}_r^a + \mathcal{U}_a^a)\cos(\omega_s^a\tau + \phi_a), \tag{2.4a}$$

$$\overline{v}_{2s}(\tau) = \frac{\delta v_{2s}}{\varepsilon_r c_2} = (\mathcal{V}_r^r + \mathcal{V}_a^r)\sin(\omega_s^r\tau + \phi_r) + (\mathcal{V}_r^a + \mathcal{V}_a^a)\sin(\omega_s^a\tau + \phi_a). \tag{2.4b}$$

The post-shock mode amplitudes $\mathcal{U}_{r,a}^{r,a}$ and $\mathcal{V}_{r,a}^{r,a}$ are unknown functions of θ^r and θ^a to be determined. Note that in Eqs. (2.3) and (2.4), the transverse coordinate dependence is omitted, $\sim\cos(k_y y)$ for the longitudinal and $\sim\sin(k_y y)$ for the transverse velocity field, as it is not affected by the shock passage due to the periodic symmetry in the transverse direction. To distinguish between the different contributions, the subscripts

r, a refer to the nature of the perturbation, rotational or acoustic, respectively, while the superscripts r, a refer to the nature of the upstream mode generating the corresponding perturbation, rotational-entropic or acoustic, respectively. As such, the rotational streamwise amplitude $\mathcal{U}_r(\theta^r, \theta^a)$ is conveniently decomposed into components associated with the upstream rotational-entropic wave $\mathcal{U}_r^r = \mathcal{U}_r^r(\theta^r)$ and the acoustic mode $\mathcal{U}_r^a = \mathcal{U}_r^a(\theta^a)$, with the superposition of modes rendering $\mathcal{U}_r = \mathcal{U}_r^r + \mathcal{U}_r^a$. The amplitude of the downstream acoustic mode can likewise be expressed as $\mathcal{U}_a(\theta^r, \theta^a) = \mathcal{U}_a^r(\theta^r) + \mathcal{U}_a^a(\theta^a)$, with the transverse velocity being similarly decomposed.

The long-time amplitudes of the different modes are computed using the perturbed Rankine-Hugoniot (RH) equations and linearized Euler equations. The isolated-shock boundary condition is applied far downstream of the shock. The boundary condition at the shock front is derived from the linearized RH jump conditions, which are evaluated at the mean shock front location based on the post-shock state characterized by $\mathcal{R}$, $\beta = c_2/c_1$ and $\mathcal{M}_2$, along with the normalized RH-slope parameters

$$\Gamma = u_2^2 \frac{\partial \rho_2}{\partial p_2}\bigg|_{\rho_1, p_1}, \quad \Gamma_\rho = \frac{\Gamma}{u_1^2}\frac{\partial p_2}{\partial \rho_1}\bigg|_{\rho_2, p_1} \quad \text{and} \quad \Gamma_p = \Gamma \frac{\partial p_2}{\partial p_1}\bigg|_{\rho_1, \rho_2}, \tag{2.5}$$

which are computed using the Combustion Toolbox (Cuadra *et al.* 2024), thereby yielding

$$\overline{u}_{2s} = \frac{1+\Gamma}{2\mathcal{M}_2}\overline{p}_{2s} - \frac{\mathcal{M}_2\mathcal{R}\,(1+\Gamma_\rho)}{2}\overline{\rho}_{1s} + \frac{1}{\beta}\overline{u}_{1s} - \frac{1+\Gamma_p}{2\beta^2\mathcal{M}_2\mathcal{R}}\overline{p}_{1s}, \tag{2.6a}$$

$$\overline{v}_{2s} = \frac{1}{\beta}\overline{v}_{1s} - \mathcal{M}_2\,(\mathcal{R}-1)\,\frac{\partial \overline{\xi}_s}{\partial \overline{y}}. \tag{2.6b}$$

In Eq. (2.6), to ensure that thermochemical equilibrium is reached, the thickness of the vibrational nonequilibrium region ℓ_T must be much smaller than the inverse of the transverse wave number k_y^{-1}, i.e., $k_y \ell_T \ll 1$. If upstream density deviations are positively correlated with rotational disturbances, i.e., $\varepsilon_e/\varepsilon_r > 0$, they contribute to reduce the post-shock streamwise velocity perturbation. The opposite occurs for negatively correlated disturbances. Note also that, for strong shocks $\mathcal{M}_1 \gg 1$, density disturbances (either entropic or acoustic) become more relevant because the influence of velocity and pressure perturbations diminish as they are proportional to $\beta^{-1} \ll 1$ and $\beta^{-2} \ll 1$, respectively. To obtain the value of the perturbation amplitudes downstream, linear superposition can be applied to independently solve the sound wave equation for $\overline{p}_2$ and Eq. (2.6) for the two upstream sources of disturbances.

The weak isotropic turbulence in the pre-shock gas can be modeled as a linear superposition of incident rotational-entropic and acoustic waves, with the corresponding amplitudes ε_r, ε_e and ε_a varying according to an isotropic energy spectrum $E(k) = \varepsilon^2(k)$. To compute the statistical averages downstream, the correlation between the different modes must be specified. In what concerns the relation between entropic and rotational disturbances, Mahesh *et al.* (1997) has addressed the case ε_e proportional to $\pm\varepsilon_r/\mathcal{M}_1$. However, Morkovin (1962) correlates $\varepsilon_e \sim \varepsilon_r \mathcal{M}_1$, so that the entropic contribution would be much more important at high Mach numbers. In this work, where turbulence amplification ratio is computed for a fixed Mach number $\mathcal{M}_1 = 5$, the correlation between different modes is readily given by

$$\langle \chi \rangle = \frac{\langle \delta\rho_1^e \delta u_1^r \rangle}{\langle \delta u_1^r \delta u_1^r \rangle}\frac{\langle c_1 \rangle}{\langle \rho_1 \rangle}, \tag{2.7}$$

which is extracted from the numerical characterization of the upstream turbulence flow.

As for the acoustic influence, the correlation with vorticity disturbances differs due to their distinct nature as traveling waves. Therefore, the impact of the acoustic waves in the TKE can be evaluated separately, with the total contribution being simply computed as the weighted sum of the respective parts. For this, we define the dimensionless variable $\eta \sim \varepsilon_a^2/\varepsilon_r^2$, which, in terms of turbulent variables, reads as

$$\eta = \frac{\langle \delta u_{1a}^2 \rangle + \langle \delta v_{1a}^2 \rangle + \langle \delta w_{1a}^2 \rangle}{\langle \delta u_{1r}^2 \rangle + \langle \delta v_{1r}^2 \rangle + \langle \delta w_{1r}^2 \rangle}, \tag{2.8}$$

where $\langle \delta u_{1a}^2 \rangle, \langle \delta v_{1a}^2 \rangle$ and $\langle \delta w_{1a}^2 \rangle$ denote the averaged dimensional value of the three orthogonal contributions of the acoustic velocity field ahead of the shock. Correspondingly, $\langle \delta u_{1r}^2 \rangle, \langle \delta v_{1r}^2 \rangle$ and $\langle \delta w_{1r}^2 \rangle$ refer to upstream rotational perturbations.

Finally, the total TKE amplification factor, K, can be defined as

$$K = \frac{\langle \delta u_2^2 \rangle + \langle \delta v_2^2 \rangle + \langle \delta w_2^2 \rangle}{\langle \delta u_1^2 \rangle + \langle \delta v_1^2 \rangle + \langle \delta w_1^2 \rangle} = \beta^2 \frac{\langle \overline{u}_2^2 \rangle + \langle \overline{v}_2^2 \rangle + \langle \overline{w}_2^2 \rangle}{\langle \overline{u}_1^2 \rangle + \langle \overline{v}_1^2 \rangle + \langle \overline{w}_1^2 \rangle} = \frac{K^r(\chi) + \eta K^a}{1 + \eta}, \tag{2.9}$$

where the factor β^2 appears because dimensionless velocity perturbations are scaled with the local speed of sounds, which change across the shock. The last equality corresponds to the linear superposition of the upstream rotational and acoustic contributions, whose intermode relations, defined as $\varepsilon_e/\varepsilon_r$ and $\varepsilon_a/\varepsilon_r$ for monofrequency disturbances, are included in K through the coefficients χ, which is internal to the computation of K^r, and η, which is factored out in the weighted sum of contribution for K^a. Likewise, this can be extended for the streamwise and transverse components of K.

3. Direct numerical simulations

The DNSs have been carried out with the Hypersonics Task-based Research (HTR) solver (Di Renzo *et al.* 2020; Di Renzo & Pirozzoli 2021; Di Renzo 2022), numerically integrating the single-component compressible Navier-Stokes equations. In this formulation, the temperature-dependent viscosity is evaluated with Sutherland's law specialized for air, whereas the thermal conductivity of the gas is determined using a constant Prandtl number of 0.71. The frozen chemical composition of the gas comprises 79% molecular nitrogen and 21% molecular oxygen on a molar basis. Two thermodynamic models are considered in these calculations pertaining to the description of the internal energy modes of air. The first model treats air as a calorically perfect diatomic gas whose constant-pressure heat capacity is constant and equal to $c_p = 7/2\mathcal{R}^0$, whereas the second represents air as a thermally perfect gas with equilibrium vibrational excitation. For the latter model, the constant-pressure heat capacity is evaluated using a nine-coefficient polynomial particularized for dry air absent argon (McBride *et al.* 2002).

The conservation equations corresponding to mass, momentum and total energy are discretely solved using conservative finite differences on Cartesian grids. The inviscid fluxes are discretized using a hybrid reconstruction scheme that utilizes a skew-symmetric formulation (Pirozzoli 2010) in smooth regions of the flow and a WENO5-JS reconstruction scheme in the vicinity of discontinuities. The switch between the two schemes is governed by a directional shock sensor based on the TENO stencil selection process (Williams *et al.* 2022). The diffusion fluxes are discretized using a second-order central formulation written in conservative form. The resulting set of ordinary differential equations is advanced in time using a third-order strong stability–preserving Runge-Kutta scheme (Gottlieb *et al.* 2001).

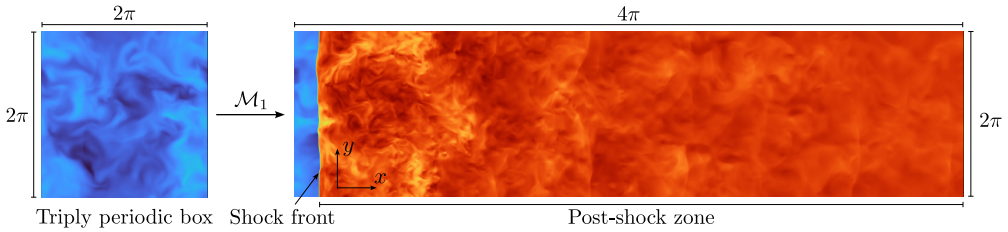

FIGURE 2. A schematic of a 3D DNS in the xy-plane showcasing isotropic turbulence generated by a triply periodic box and advecting at a mean Mach number $\mathcal{M}_1$ toward the STI domain.

The computational framework for the DNS consists of two distinct calculations executed concurrently; Figure 2 provides a schematic view of a 3D DNS in the xy-plane. The first simulation, functioning as a turbulence generator, comprises a triply periodic cubic computational domain with dimensions $2\pi \times 2\pi \times 2\pi$ wherein HIT is forced to sustain TKE. The HIT domain is discretized with 800^3 points. The turbulence forcing is inspired by the work of Petersen & Livescu (2010) and allows us to impose the dilatational and solenoidal turbulent kinetic energy of the flow separately. The latter calculation corresponds to the STI itself, consisting of a computational domain with dimensions $4\pi \times 2\pi \times 2\pi$. The computational domain is periodic in the traversal directions, namely y and z, and it is discretized with 1600×800^2 points in the streamwise and transverse directions, respectively.

Characteristic boundary conditions are imposed at both the upstream and downstream boundaries (Poinsot & Lele 1992). In particular, the supersonic inflow condition enforces the velocity, temperature and pressure fluctuations computed in the turbulence generator and superimposed on the bulk convective velocity corresponding to the characteristic Mach number of the interaction. A subsonic outflow boundary condition, which weakly imposes the far-field static pressure of the flow, is utilized at the downstream boundary of the computational domain. The normal shock is nominally positioned at a distance of approximately 0.5π downstream of the inflow, with the outflow back pressure weakly imposed to preserve this nominal shock wave position. The pre-computed back pressure to be weakly imposed at the outflow, which produces zero mean drifting in the shock location, is determined iteratively following the procedure of Larsson & Lele (2009). The shock is considered stationary when its mean drift velocity is at least four orders of magnitude smaller than the incoming mean flow velocity.

4. Results and discussion

Utilizing the theoretical and computational frameworks outlined in the previous sections, we now examine the impact of upstream compressibility and vibrational excitation on canonical STI at Mach number $\mathcal{M}_1 = 5$ and Taylor-scale Reynolds number $Re_\lambda = 40$. The flow setups discussed throughout the manuscript are summarized in Table 1 and are obtained by various permutations of two values of turbulent Mach numbers, $\mathcal{M}_t = [0.2, 0.4]$, three values of dilatational-to-solenoidal TKE ratio, $\eta = [0.001, 0.05, 0.1]$, and two equations of state (EoS), namely the ideal gas EoS (cases labeled with C) and thermally perfect gas EoS (cases labeled with G). Aside from the case parameters, the table summarizes the post-shock turbulence statistics, averaged over time, and the transverse y- and z-directions. Following the methodology in Chen & Donzis (2019), the lo-

Case	$\mathcal{M}_t$	η	γ	$10^3\langle\chi\rangle$	K	K^{LIA}	ΔK^{LIA}[%]	R_{11}	R_{11}^{LIA}	$\Delta R_{11}^{\mathrm{LIA}}$[%]	R_{22}	R_{22}^{LIA}	$\Delta R_{22}^{\mathrm{LIA}}$[%]
C1	0.20	0.05	1.4	-0.94	1.81	2.20	21.68	2.64	1.83	-30.53	1.42	2.39	68.07
C2	0.20	0.10	1.4	-4.90	2.21	2.59	16.99	2.95	2.34	-20.53	1.86	2.71	45.49
C3	0.40	0.05	1.4	0.39	1.61	2.20	36.43	2.33	1.83	-21.59	1.25	2.38	90.51
C4	0.40	0.10	1.4	-1.82	1.99	2.57	29.27	2.72	2.33	-14.38	1.65	2.69	63.29
C5	0.20	0.001	1.4	-1.43	1.46	1.81	23.98	1.93	1.31	-32.21	1.23	2.06	67.57
G1	0.20	0.05	$\gamma(T)$	-4.15	2.02	2.26	12.05	2.77	1.75	-36.77	1.70	2.52	48.19
G2	0.20	0.10	$\gamma(T)$	-8.02	2.31	2.63	13.95	3.16	2.21	-30.02	1.93	2.84	47.29
G3	0.40	0.05	$\gamma(T)$	-8.40	1.67	2.28	36.71	2.34	1.77	-24.21	1.32	2.54	92.26
G4	0.40	0.10	$\gamma(T)$	-9.91	2.05	2.64	28.81	2.95	2.22	-24.72	1.57	2.85	81.57

TABLE 1. Comparison of post-shock turbulence statistics at the local maximum of R_{11}, obtained from DNS and LIA. All cases are conducted at $\mathcal{M}_1 = 5$ and $Re_\lambda = 40$. The parameters $\Delta\phi^{\mathrm{LIA}}$ denote the percentile differences between LIA and DNS statistics, where $\phi = K, R_{11}$ and R_{22}.

cation where the streamwise Reynolds stress R_{11} reaches its local post-shock maximum is used to define the far-field solution in the DNS, as outlined below.

Figure 3 presents the TKE ratio K (panels a, c, d) and the streamwise Reynolds stress tensor component amplification ratio R_{11} (panel b). The averages are plotted as a function of the normalized streamwise coordinate $\lambda^{-1}(x - x_s)$, where λ is the Taylor microscale. As the flow progresses toward the shock, a gradual decay occurs due to dissipation until it reaches the shock location, indicated by the green shaded area; the prominent peaks that appear in this region are due to the strong fluctuations in the shock position. After this, only R_{11} (panel b) exhibits a local minimum and a gradual increase associated with a transfer from the pressure field to the velocity field (Lee *et al.* 1993). The contribution of viscous effects, which are always present, is found to compensate for the increasing value of R_{11} at the location where the maximum value is observed.

In Figure 3(a), cases C3 and C4, corresponding to η values of 5% and 10%, respectively, show a relative increase in K of approximately 24%. This trend persists regardless of the turbulent Mach number $\mathcal{M}_t$, as seen in cases C1 and C4, which exhibit a similar relative amplification of around 22%. Notably, when the upstream turbulence is almost solenoidal, namely for case C5 in panel c, K decreases by about 50% compared to case C2. This underscores the pivotal role that upstream dilatational fluctuations play, characterized by η. The increase in TKE components can be attributed to the higher acoustic energy content immediately after the shock, which, as previously commented, is transferred into kinetic energy in the near-field after the shock. The effect of vibrational excitation is illustrated in Figure 3(d) and summarized in Table 1. The comparison between the perfect gas (C-series) and thermally perfect gas (G-series) cases reveals that temperature-dependent variations in the specific heat ratio, $\gamma(T)$, further modulate K. For example, in cases G3 and G4, the amplification of K is approximately 4% higher than in their perfect gas counterparts. This occurs due to the stronger shock compression in the thermally perfect gas cases compared to the calorically perfect approximation, which enhances the post-shock rotational kinetic energy component. These findings suggest that, while the dilatational content remains the dominant factor of turbulence amplification, the endothermic effects also exert a secondary but significant impact.

The trends discussed above are well captured by linear theory, despite that the LIA values used in this study correspond to constant far-field solutions, which, unlike DNS results that are affected by viscous dissipation, do not decay downstream. For clarity, these LIA values are represented by a single bar symbol. For instance, LIA anticipates a 16% (27%) amplification of K (R_{11}) for cases C3 and C4 when increasing η, which

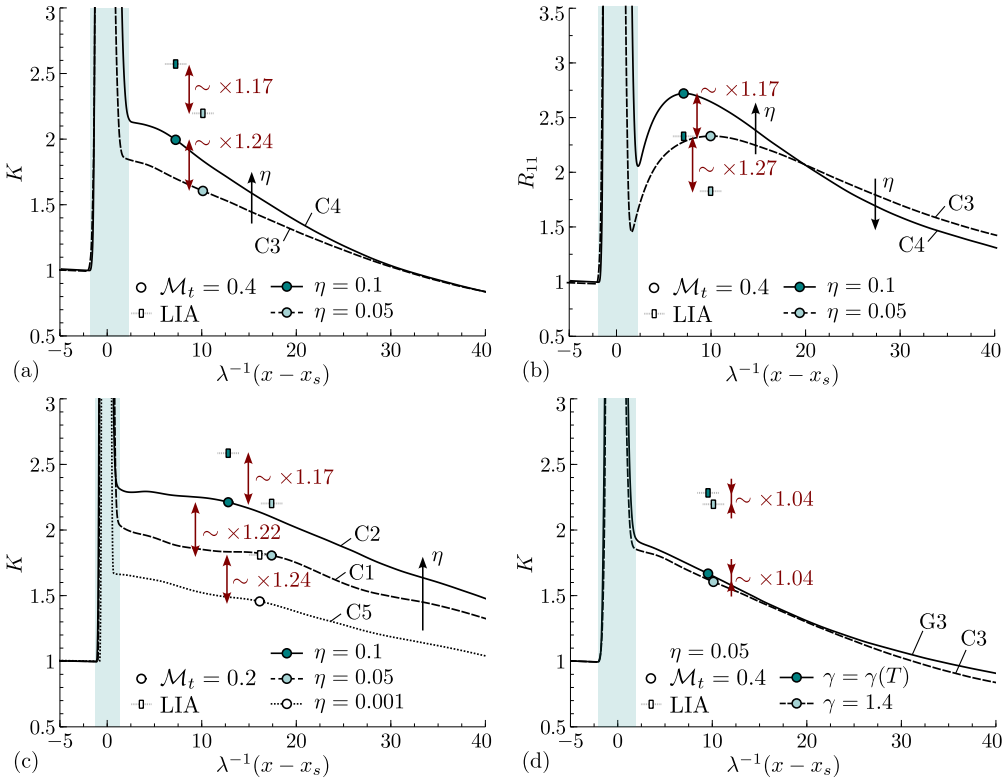

FIGURE 3. Evolution of the TKE amplification K (panels a, c, d) and its streamwise component R_{11} (panel b) under different conditions, as specified in Table 1.

compares reasonably well with the 24% (17%) observed in DNS. Regarding upstream entropic fluctuations, their contribution remains minimal in all the cases studied due to the small relative amplitude, namely $|\langle\chi\rangle| \approx 10^{-3}$. From a theoretical perspective, LIA predicts a strong dependence of K on χ: K increases (decreases) with negative (positive) values of χ due to constructive (destructive) interference between vortical and entropic waves. In the most influential scenario, where $\langle\chi\rangle \approx \pm 1 \cdot 10^{-2}$, LIA anticipates variations in $(1+\eta)^{-1}K^r$ of only about $\pm 2.6\%$. This is considerably smaller than the observed amplification of up to 48% resulting from upstream acoustic fluctuations through $\eta(1+\eta)^{-1}K^a$ under the tested conditions.

Despite the overall agreement in relative amplifications, notable discrepancies arise when directly comparing LIA and DNS results. For instance, in case C2 (panel c), LIA overestimates K by 17% compared to DNS. These discrepancies become more pronounced with as increasingly turbulent Mach number $\mathcal{M}_t$, likely due to nonlinear and viscous effects, which are not considered in the LIA. Additionally, far-field LIA values exclude the contribution of acoustic evanescent waves associated with low-frequency disturbances. Finally, the mean shock thickness, represented by the green shaded area, is found to increase with the upstream dilatational-to-solenoidal ratio, η. This observation aligns with previous findings by Mahesh *et al.* (1997), in which shock broadening was attributed to density-entropic fluctuations upstream of the shock, in contrast to the density-acoustic disturbances that, in our setup, dominate ahead of the shock for $\eta^{1/2} \gg \chi$.

5. Conclusions

The present study analyzes the effects of upstream density perturbations and equilibrium vibrational excitation on the statistics of a Mach-5 shock wave/homogeneous-isotropic-turbulence interaction. These effects are jointly analyzed using direct numerical simulations (DNSs) and linear interaction analysis (LIA). In particular, multiple DNS are conducted, varying the pre-shock turbulent Mach number, the percentage of turbulent kinetic energy (TKE) associated with dilatational modes and the degree of internal-energy excitation. For that purpose, a fully consistent LIA formulation is developed to account for acoustic, entropy and rotational disturbances in the upstream flow.

Even a small presence of dilatational modes in the upstream turbulence can significantly impact the shock-turbulence interaction (STI) dynamics at Mach 5. DNS results reveal that increasing the dilatational TKE for 5% to 10% of the solenoidal TKE enhances velocity perturbation amplification due to the shock by about 24%. Including high-temperature endothermic effects such as vibrational excitation further increases TKE amplification by approximately 4%, with this effect expected to grow at higher Mach numbers. In terms of the absolute values of TKE, LIA slightly overpredicts the TKE amplification, as is commonly observed for canonical STI. This discrepancy is likely due to factors such as the turbulent Mach number and the relatively low Reynolds number of the simulated flows, though further studies are needed to confirm this hypothesis. When assessing the relative impact of density and high-temperature effects on STI, both the theoretical and numerical approaches yield remarkably similar estimates. This outcome is particularly notable given the significantly lower computational cost of LIA.

Acknowledgments

We acknowledge the CINECA award under the ISCRA initiative, for the availability of high-performance computing resources and support.

REFERENCES

Chen, C. H. & Donzis, D. A. 2019 Shock–turbulence interactions at high turbulence intensities. *J. Fluid Mech.* **870**, 813–847.

Clarke, J. F. 1991 Chemical reactions in high-speed flows. *Philos. T. Roy. Soc. A* **335**, 161–199.

Cuadra, A. 2023 Development of a wide-spectrum thermochemical code with application to planar reacting and non-reacting shocks. Ph.D. Thesis, Univ. Carlos III de Madrid, Madrid, Spain.

Cuadra, A., Huete, C. & Vera, M. 2024 Combustion Toolbox: An open-source thermochemical code for gas- and condensed-phase problems involving chemical equilibrium. arXiv:2409.15086 [physics.chem-ph].

Cuadra, A., Vera, M., Di Renzo, M. & Huete, C. 2023 Linear theory of hypersonic shocks interacting with turbulence in air. *AIAA Paper* 2023–0075.

Di Renzo, M. 2022 HTR-1.3 solver: Predicting electrified combustion using the Hypersonic Task-based Research solver. *Comput. Phys. Commun.* **272**, 108247.

Di Renzo, M., Fu, L. & Urzay, J. 2020 HTR solver: An open-source exascale-oriented task-based multi-GPU high-order code for hypersonic aerothermodynamics. *Comput. Phys. Commun.* **255**, 107262.

Di Renzo, M. & Pirozzoli, S. 2021 HTR-1.2 solver: Hypersonic Task-based Research solver version 1.2. *Comput. Phys. Commun.* **261**, 107733.

Gottlieb, S., Shu, C.-W. & Tadmor, E. 2001 Strong stability-preserving high-order time discretization methods. *Siam Rev.* **43**, 89–112.

Grube, N. E. & Martín, M. P. 2023 Compressibility effects on Reynolds stress amplification and shock structure in shock–isotropic turbulence interactions. *J. Fluid Mech.* **958**, A1.

Huete, C., Cuadra, A., Vera, M. & Urzay, J. 2021 Thermochemical effects on hypersonic shock waves interacting with weak turbulence. *Phys. Fluids* **33**, 086111.

Huete, C., Velikovich, A. & Wouchuk, J. 2011 Analytical linear theory for the interaction of a planar shock wave with a two- or three-dimensional random isotropic density field. *Phys. Rev. E* **83**, 056320.

Huete, C., Wouchuk, J. & Velikovich, A. 2012 Analytical linear theory for the interaction of a planar shock wave with a two- or three-dimensional random isotropic acoustic wave field. *Phys. Rev. E* **85**, 026312.

Jamme, S., Cazalbou, J.-B., Torres, F. & Chassaing, P. 2002 Direct numerical simulation of the interaction between a shock wave and various types of isotropic turbulence. *Flow Turbul. Combust.* **68**, 227–268.

Larsson, J. & Lele, S. K. 2009 Direct numerical simulation of canonical shock/turbulence interaction. *Phys. Fluids* **21**, 126101.

Lee, S., Lele, S. K. & Moin, P. 1993 Direct numerical simulation of isotropic turbulence interacting with a weak shock wave. *J. Fluid Mech.* **251**, 533–562.

Mahesh, K., Lele, S. K. & Moin, P. 1997 The influence of entropy fluctuations on the interaction of turbulence with a shock wave. *J. Fluid Mech.* **334**, 353–379.

McBride, B. J., Zehe, M. J. & Gordon, S. 2002 NASA Glenn coefficients for calculating thermodynamic properties of individual species. *Tech. Rep.*, NASA.

Morkovin, M. V. 1962 Effects of compressibility on turbulent flows. *Méch. Turbul.* **367**, 380.

Petersen, M. R. & Livescu, D. 2010 Forcing for statistically stationary compressible isotropic turbulence. *Phys. Fluids* **22**, 116101.

Pirozzoli, S. 2010 Generalized conservative approximations of split convective derivative operators. *J. Comput. Phys.* **229**, 7180–7190.

Poinsot, T. J. & Lele, S. K. 1992 Boundary conditions for direct simulations of compressible viscous flows. *J. Comput. Phys.* **101**, 104–129.

Urzay, J. & Di Renzo, M. 2021 Engineering aspects of hypersonic turbulent flows at suborbital enthalpies. *Annual Research Briefs*, Center for Turbulence Research, Stanford University, pp. 7–32.

Vincenti, W. & Kruger, C. H. 1965 Introduction to Physical Gas Dynamics. Krieger Publishing.

Williams, C. T., Di Renzo, M. & Moin, P. 2022 Computational framework for direct numerical simulation of shock-turbulence interaction in thermochemical nonequilibrium. *Annual Research Briefs*, Center for Turbulence Research, Stanford University, pp. 203–216.